Polymeric carbon nitride coupled with a molecular thiomolybdate catalyst: exciton and charge dynamics in light-driven hydrogen evolution

Ashwene Rajagopal,[a] Elham Akbarzadeh,[a] Chunyu Li,[b,c] Dariusz Mitoraj,[d] Igor Krivtsov,[d,*]

Christiane Adler,[d] Thomas Diemant,[e] Johannes Biskupek,[f] Ute Kaiser,[f] Changbin Im,[d] Magdalena

Heiland,[a] Timo Jacob,[d,g,h] Carsten Streb,[a,g,h]* Benjamin Dietzek,[b,c,i] * Radim Beranek[d,*]

[a]   Institute of Inorganic Chemistry I, Ulm University, Albert-Einstein-Allee 11, 89081 Ulm, Germany

[b]   Institute of Physical Chemistry and Abbe Center of Photonics, Friedrich Schiller University Jena, Lessingstr. 10, 07743 Jena, Germany

[c]   Department Functional Interfaces, Leibniz Institute of Photonic Technology (IPHT), Albert-Einstein-Str. 9, 07745 Jena, Germany

[d]   Institute of Electrochemistry, Ulm University, Albert-Einstein-Allee 47, 89081 Ulm, Germany

[e]   Institute of Surface Chemistry and Catalysis, Ulm University, Albert-Einstein-Allee 47, 89081 Ulm, Germany

[f]   Electron Microscopy of Materials Science, Central Facility for Electron Microscopy, Ulm University, Albert-Einstein-Allee 11, 89081, Ulm, Germany

[g]   Helmholtz-Institute-Ulm (HIU), Helmholtzstr. 11, 89081, Ulm, Germany

[h]   Karlsruhe Institute of Technology (KIT), P.O. Box 3640, 76021, Karlsruhe, German

[i]   Center for Energy and Environmental Chemistry Jena (CEEC Jena), Philosophenweg 7a, 07743 Jena, Germany

*Corresponding authors: igor.krivtsov@uni-ulm.de, carsten.streb@uni-ulm.de,

benjamin.dietzek@uni-jena.de, radim.beranek@uni-ulm.de

Abstract

Solar hydrogen evolution from water is a necessary step to overcome the challenges of rising energy demand and associated environmental concerns. Low-cost photocatalytic architectures based on polymeric light absorbers coupled to highly efficient molecular catalysts might represent an attractive platform to address this issue. However, to-date, our mechanistic knowledge of these systems is still largely underdeveloped. In this study, a molecular molybdenum sulfide hydrogen evolving catalyst, $[Mo_3S_{13}]^{2-}$, is loaded onto polymeric carbon nitride (CN_x) photoabsorber by impregnation. The resulting composite shows enhanced photocatalytic activity for hydrogen evolution compared to pristine CN_x under monochromatic visible light ($\lambda = 420$ nm) irradiation in the presence of sacrificial reducing agents. The light-driven dynamics of excitons and charges involved in hydrogen evolution catalysis were studied by a combination of spectroscopic (steady-state and time-resolved photoluminescence, femtosecond time-resolved transient absorption) and photoelectrochemical (open-circuit photopotential transients) methods. We demonstrate that the molecular molybdenum sulfide catalyst, at optimum loading (10 wt% nominal), improves the charge separation in the CN_x absorber by facilitating the depopulation of emissive (band-edge) or non-emissive (shallow trap) states, followed by an effectively catalyzed transfer of electrons from the charge-separated state (deep trap) to protons in the solution. The results provide important insights into the complex interplay between polymeric light absorbers and molecular redox catalysts, indicating that the electron transfer to the catalyst occurs on relatively longer (nanosecond – seconds) time scale, as the catalyst had no impact on the ultrafast (sub-nanosecond) photoinduced kinetics in the CN_x. These findings are of crucial importance for further development of soft-matter based architectures for solar fuels production.

1. Introduction

Sunlight-driven photocatalytic hydrogen evolution reaction (HER) remains one of the greatest challenges on the way towards sustainable alternatives to fossil fuels.[1] A vast range of materials and approaches intended to tackle this goal have been investigated, and the pertinent research results have now been summarized in numerous review papers.[2-5] The challenge is far from trivial: in order to be implemented in real life, the photocatalyst must be highly active, selective and stable, and at the same time based on low-cost and abundant elements. Hence, there is a quest for replacing conventional, mostly metal oxide-based semiconductors and noble metal co-catalysts with more affordable alternatives.[6] In 2009, X. Wang *et al.* stirred the research community with the discovery of photocatalytic properties of polymeric carbon nitride (also referred in literature as melon, CN_x, C_3N_4 polymer, or g-C_3N_4).[7] This finding gave rise to a large number of publications on carbon nitride polymers modified with various co-catalysts, such as Pt and other noble metals,[8-10] metal-organic complexes,[11] metal phosphides,[12] and metal sulphides.[13] The latter received a special attention as WS_2[14] or MoS_2[15] were demonstrated to be efficient alternatives to the benchmark Pt catalysts for HER. However, in such layered metal sulfides only the undercoordinated edge sulfur atoms act as active sites for hydrogen evolution, while the rest of their 2D structure is inert.[16] This finding prompted the search for molecular[17] or nanoparticulate forms[18] of these materials, with the aim to maximize the number of exposed active species. The $[Mo_3S_{13}]^{2-}$ molecular clusters have been established as one of such promising co-catalysts for dark electrocatalytic[16,19-22] and photocatalytic HER under heterogeneous[23-25] and homogeneous conditions.[26,27] Anchoring of the cluster onto various solid catalyst supports or light absorbers is straightforward and has been demonstrated for TiO_2,[28] carbon materials,[20,21] and recently also for polymeric carbon nitride-based material.[25] More specifically, X. Wang *et al.* have coupled $[Mo_3S_{13}]^{2-}$ $[=\{Mo_3\}]$ to protonated mesoporous carbon nitride with rod-like morphology (diameter ca. 1 μm), and the activity in photocatalytic HER of the hybrid was reported to be comparable with that of Pt-modified mesoporous carbon nitride using lactic acid as sacrificial electron donor.[25] However, to the best of our knowledge, no insight into the

interaction and charge transfer processes between the support and co-catalyst has been presented so far. Herein, we demonstrate that {Mo$_3$} deposited onto conventional polymeric carbon nitride can effectively catalyse visible light-driven hydrogen evolution using methanol as a reducing agent. Furthermore, using a combination of spectroscopic (steady-state and time-resolved photoluminescence, transient absorption) and photoelectrochemical (open-circuit photopotential) tools we shed light on the complex interplay between the carbon nitride light absorber and the molecular {Mo$_3$} catalyst influencing the exciton dynamics and the kinetics of catalytic turnover in light-driven hydrogen evolution.

2. Experimental

2.1 Materials

Melamine, hexachloroplatinic acid hydrate (H$_2$PtCl$_6$ nH$_2$O), triethanolamine (TEOA) were purchased from Aldrich, methanol was supplied by VWR chemicals. (NH$_4$)$_6$[Mo$_7$O$_{24}$] × 4H$_2$O and methanol for catalysis was purchased from Aldrich. Ammonium polysulfide was purchased from Chemos GmbH.

2.2 Synthesis

Synthesis of polymeric carbon nitride: The polymeric carbon nitride (CN$_x$) was prepared by thermal polycondensation of 30 g melamine at 530 ℃ for 4h in a lid-covered crucible.

Synthesis of (NH$_4$)$_2$[Mo$_3$S$_{13}$] × 2H$_2$O: The thiomolybdate (NH$_4$)$_2$[Mo$_3$S$_{13}$] × 2H$_2$O was prepared by a modification of the synthesis reported by Müller *et al.*[29] (NH$_4$)$_6$[Mo$_7$O$_{24}$] × 4H$_2$O (4.0 g, 3.2 mmol) was dissolved in water (20 ml) in a round bottom flask, then ammonium polysulfide ((NH$_4$)$_2$S$_x$) solution (120 ml, 25 wt.-%) was added to it and fitted with condenser. The solution was heated to 96 °C for five days with slow stirring. Dark-red crystals of (NH$_4$)$_2$[Mo$_3$S$_{13}$] × 2H$_2$O formed and were removed by filtration, washed with water, ethanol, carbon disulfide and ether. Finally, the product was air-dried. Yield: 5.6 g (7.16 mmol, 97.9 % based on Mo).

Synthesis of Na$_2$[Mo$_3$S$_{13}$] × 5H$_2$O: Na$_2$[Mo$_3$S$_{13}$] x 5H$_2$O was synthesized as follows. (NH$_4$)$_2$[Mo$_3$S$_{13}$] × 2H$_2$O (3.02 g, 3.86 mmol) was suspended in an aqueous NaOH solution (1 wt.-%, 40 ml) and stirred under reduced pressure (20 mbar) for 2 h, in order to remove ammonium as NH$_3$ gas. The resulting dark red solution was filtered into an aqueous NaCl solution (10 wt.-%, 100 ml). After 12 h, the precipitated product was isolated by filtration, washed with 2-propanol and diethyl ether, and dried *in vacuo* at room temperature to give red-brown powder of Na$_2$[Mo$_3$S$_{13}$] × 5H$_2$O. Yield: 3.20 g (3.78 mmol, 95.9 % based on Mo).

Synthesis of CN$_x$-{Mo$_3$} composites:

CN$_x$-{Mo$_3$} hybrids were synthesized through a two-step deposition process at room temperature. In a typical procedure, 20 mg of as-prepared CN$_x$ was dispersed in 20 mL of methanol by ultrasonication for 3 h to prepare a homogenous suspension. Then, a measured amount of Na$_2$[Mo$_3$S$_{13}$] (soluble in methanol) was added to it and stirred for 24 h. The solid was collected by centrifugation and three times washed with methanol to remove the excess of {Mo$_3$}. Finally, the obtained precipitates were air-dried at room temperature under ambient conditions giving CN$_x$-{Mo$_3$}. Different loadings of {Mo$_3$} were deposited onto the CN$_x$ material.

Synthesis of Pt-modified CN$_x$: The platinized CN$_x$ (CN$_x$-Pt) was prepared as a benchmark photocatalyst using a photodeposition method. For this, the CN$_x$ powder (0.2 g) was suspended in 20 mL H$_2$O:MeOH (9:1, v:v) solution containing hexachloroplatinic acid (4 mg), ultrasonicated for 1h, bubbled with argon gas and irradiated for 30 min with a 150W Xe-lamp equipped with a KG3 (Schott) heat filter. Subsequently, the powder was washed by centrifugation and dried overnight at 60 ℃.

2.3 Characterization

ICP-AES. The actual loading of molybdenum sulfide cluster in the samples was determined using an inductively coupled plasma atomic emission spectrometer (ICP-AES, Horiba Jobin Yvon). For this, the Mo-CN$_x$-{Mo$_3$} samples were dissolved in 1M KOH at 100 °C in autoclave.

FT-IR spectroscopy: FT-IR spectroscopy was performed on a Shimadzu FT-IR-8400S spectrometer. Samples were prepared as KBr pellets.

X-ray powder diffraction (XRD): XRD was collected on a Rigaku XRD-6000 diffractometer using Cu Kα radiation ($\lambda = 0.154$ nm).

Thermogravimetric analysis (TGA): TGA was performed on a Setaram Setsys CS Evo (30 - 1000°C at 10K/min, 50 ml/min air, Graphite crucible 0.5 ml).

X-ray photoelectron spectroscopy (XPS): XPS measurements were performed with a PHI 5800 MultiTechnique ESCA system using monochromatized Al Kα radiation (250 W, 15 kV) and pass energies of 93.9 and 29.35 eV for survey and detail spectra, respectively, at a detection angle of 45°. The measurements were analyzed with the CasaXPS software, using a Shirley-type background and peaks of Gaussian-Lorentzian peak shape (70% G / 30% L).

Transmission Electron Microscopy (TEM): The samples were dispersed in ethanol (supersonic bath) and drop-cast on holey carbon TEM grids. The TEM investigations were carried out using an image-side corrected FEI Titan 80-300 microscope operating at 80 kV. Imaging included diffraction pattern from selected areas and high resolution (HR) TEM. Energy filtered imaging exploiting absorption edges for elemental mapping were acquired using a Gatan GIF Quantum energy filter attached to microscope.

Diffuse reflectance spectroscopy (DRS): Diffuse reflectance UV-vis spectra of solids were recorded using a Shimadzu UV2600 UV-vis spectrophotometer from the samples pressed in pellets with $BaSO_4$.

Spectroscopic characterization: Polymeric carbon nitride suspensions for spectroscopic study were prepared by sonicating the carbon nitrides in deionized water ($2mg\ mL^{-1}$) for 15 min. The supernatant liquid was collected after centrifugation (10 min, 7500 rpm) and used for steady-state emission and fs-transient absorption spectroscopy.

Steady-state emission spectra ($\lambda_{ex} = 380$ nm) were recorded with a FLS980 spectrometer (Edinburgh Instruments) in a 1 cm quartz cell. Time resolved emission data were recorded using a Hamamatsu HPDTA streak camera. A Ti:sapphire laser (Tsunami, Newport Spectra-Physics GmbH) was used as the light source and a pulse selector (model 3980, Newport Spectra-Physics GmbH) was used to

reduce the repetition rate of the pulse train to 400 kHz. The emission was collected from a 1 cm cuvette in a 90° angle between the pump beam and a CHROMEX spectrograph detector. Analysis of the time-resolved emission data was performed using DecayFit software. Femtosecond (fs) transient absorption spectra were collected by using a previously reported home-built pump-probe laser system[30] based on an amplified Ti:Sapphire oscillator (Libra, Coherent Inc.). The pump pulses centered at 325 nm were generated in a collinear optical-parametric amplifier (TOPAS-C, LightConversion Ltd.). The power of the pump beam was kept at 0.15 mW before samples. The white light continuum between 450 and 785 nm used to probe the photoexcited sample is generated by focusing a part of the fundamental laser output into an eccentrically rotating CaF_2 plate. The resultant supercontinuum is delayed in time with respect to the pump beam by means of an optical delay line and the polarization between probe and pump is set at the magic angle. The data were collected from the suspensions in 1 cm cuvettes.

Photopotential measurements: 50 mg of photocatalyst were suspended in 250 μL of methanol and sonicated for 5 minutes. Then, 200 μL of the suspension was smeared onto an FTO glass by doctor blading using a scotch tape as frame and spacer. The photoelectrodes were dried at 100 °C for 15 minutes and pressed for 3 minutes at a pressure of 200 kg cm^{-2}. The photoelectrochemical setup consisted of a SP-300 BioLogic potentiostat and a three-electrode configuration using a platinum counter electrode and a Ag/AgCl (3M KCl) reference electrode. The photoelectrodes were pressed against an O-ring of the cell leaving an irradiated area of 0.5 cm². The measurements were collected under open circuit voltage conditions. The photoelectrodes were irradiated from the backside (through the FTO glass) by monochromatic light of 380 nm (Instytut Fotonowy). The measurements were conducted in a pH 7 lithium perchlorate electrolyte under argon atmosphere (solution was bubbled with Ar for 30 minutes) in the absence of any sacrificial electron donor.

2.4 Photocatalytic studies

The preliminary photocatalytic experiments showed that the nominal mass ratio of 1:10 ($\{Mo_3\}$:CN_x) was optimal for photocatalytic activity (see Electronic Supplementary Information, ESI, Fig. S1),

hence the detailed study of the photocatalytic properties was focused on this material in the following. The photocatalytic hydrogen evolution experiments were carried out using a custom-built air-cooling apparatus for maintaining room temperature (22°C) and constant irradiation of the sample. Experiments were carried out in 21 mL Schlenk tubes capped with rubber septa. 10 mg of the CN_x-based catalysts were added to the Schlenk tube equipped with magnetic stirrer. The tube was evacuated and filled with argon. A H_2O : MeOH (9 : 1, v/v) solution, with or without addition of additional sacrificial electron donor, was purged with argon. 10 mL of the degassed solution were added to the photocatalyst in the Schlenk tube under inert conditions and kept under constant irradiation from a LED source ($\lambda = 420$ nm; ca. 50 mW cm^{-2}) in air-cooled photoreactors. The gas phase of the Schlenk tube was probed by inserting a gas-tight GC syringe through the septum and the amount of hydrogen in the gas phase was quantified using headspace gas chromatography.

Gas Chromatography: Gas-chromatography (GC) was performed on a Bruker Scion GC/MS, with a thermal conductivity detector 15 (column: molecular sieve 5A 75 m $\times$ 0.53 mm, oven temperature 70 °C, flow rate 25 ml min^{-1}, detector temperature 200 °C with Argon as carrier gas. The GC was calibrated by direct injection of known amounts of H_2 gas.

3. Results and discussion

X. Wang et al. demonstrated that the interaction between the negatively charged $[Mo_3S_{13}]^{2-}$ $[=\{Mo_3\}]$ clusters and the polymeric carbon nitride surface can be reinforced by protonation of the latter, thus providing stronger electrostatic interaction.[25] However, it was shown that $\{Mo_3\}$ is also efficiently immobilized on negatively charged carbon surfaces, bearing –OH and –COOH functional groups.[16] Polymeric carbon nitride (PCN), apart from its polyheptazine structure, also possesses various functional amino-groups that have positive charges and can play an important role as anchoring sites *via* electrostatic interactions and hydrogen bonding.[31,32] One can therefore expect that $\{Mo_3\}$ would selectively attach to these surface moieties without covering the entire polymeric carbon nitride surface. According to ICP data, the actual loadings of the $Na_2[Mo_3S_{13}]$ $5H_2O$ clusters in the CN_x

samples are 0.24, 0.85 and 2.06 wt% for the nominal loadings of 2, 10 and 20 wt%, respectively. The deposition of the {Mo$_3$} clusters onto carbon nitride does not affect the support's long-range order as only a slight reduction of the intensity of the characteristic (100) and (002) maxima is observed in the composite's XRD pattern with respect to the pristine CN$_x$, which is, most likely, related to its partial exfoliation under sonication (Fig. 1a). FTIR spectra corroborate the absence of significant structural changes in CN$_x$ caused by the co-catalyst incorporation (Fig. 1b; see also a detailed discussion in ESI). However, we note the reduction of the relative intensity of the peak around 3125 cm^{-1} in the spectrum of CN$_x$-{Mo$_3$} (Fig. 1b). This can be assigned either to partial elimination of the uncondensed NH$_x$-groups caused by ultrasonication treatment or to their interaction with the {Mo$_3$} clusters. Only a small fraction of the [Mo$_3$S$_{13}$]$^{2-}$ species present in the initial solution is retained on the CN$_x$ surface after washing. XPS surface elemental analysis of the CN$_x$-{Mo$_3$} sample (10 wt% loading) allows to estimate that the Mo:N atomic ratio in the sample is only about 0.03, which implies that there is approximately one {Mo$_3$} cluster for every 13 heptazine units. XPS analysis confirms that the polymeric carbon nitride structure has not suffered significant structural changes upon {Mo$_3$} deposition. The C 1s spectrum displays two peaks located at 288.3 eV and 284.8 eV (ESI, Fig. S2). The peak with binding energy of 288.3 eV is assigned to the typical aromatic C−N=C species in the triazine rings of the CN$_x$ framework and the peak at 284.8 eV can be attributed to adventitious carbon (Fig. S2). In the N 1s spectra of the composite three peaks located at 398.7, 399.6 and 401.1 eV can be ascribed to the C−N=C, N−C$_3$ and C−NH$_x$ groups, respectively (Fig. S2).[32] As to the anchored {Mo$_3$}, the presence of Mo in the hybrid becomes evident by analysis of the spectra in the Mo 3d range. Apart of the S 2s peak at 226.7 eV, which also appears in this energy range, two Mo 3d peak doublets are detected. The first one with dominating intensity at 229.1 and 232.2 eV can be attributed to Mo^{4+} and is most probably related to the {Mo$_3$} particles (Fig. 1c).[33] The second doublet at 232.2 and 235.3 eV is most likely due to traces of Mo^{6+} formed upon partial exchange of S$_2^{2-}$ by hydroxide or water ligands. The S 2p spectrum is more informative, since it confirms the integrity of the immobilized {Mo$_3$} clusters. The S 2p spectrum can be fitted by introducing two doublet peaks (2p$_{3/2}$

and $2p_{1/2}$). The doublet at (161.9 eV and 163.1 eV) is attributed to the terminal S_2^{2-} ligands and the doublet at (163.1 eV and 164.3 eV) is assigned to the apical S^{2-} and bridging S_2^{2-} in the $[Mo_3S_{13}]^{2-}$ clusters (Fig. 1d).[16,33] Finally, the presence of sulfate species in the composite is indicated by another peak doublet at higher binding energy (168.1 and 169.3 eV), characteristic for S−O binding. We assume that the sulfate was generated during the cation exchange process from residual sulfur existing in $(NH_4)_2Mo_3S_{13}\cdot2H_2O$ (Fig. 1d).
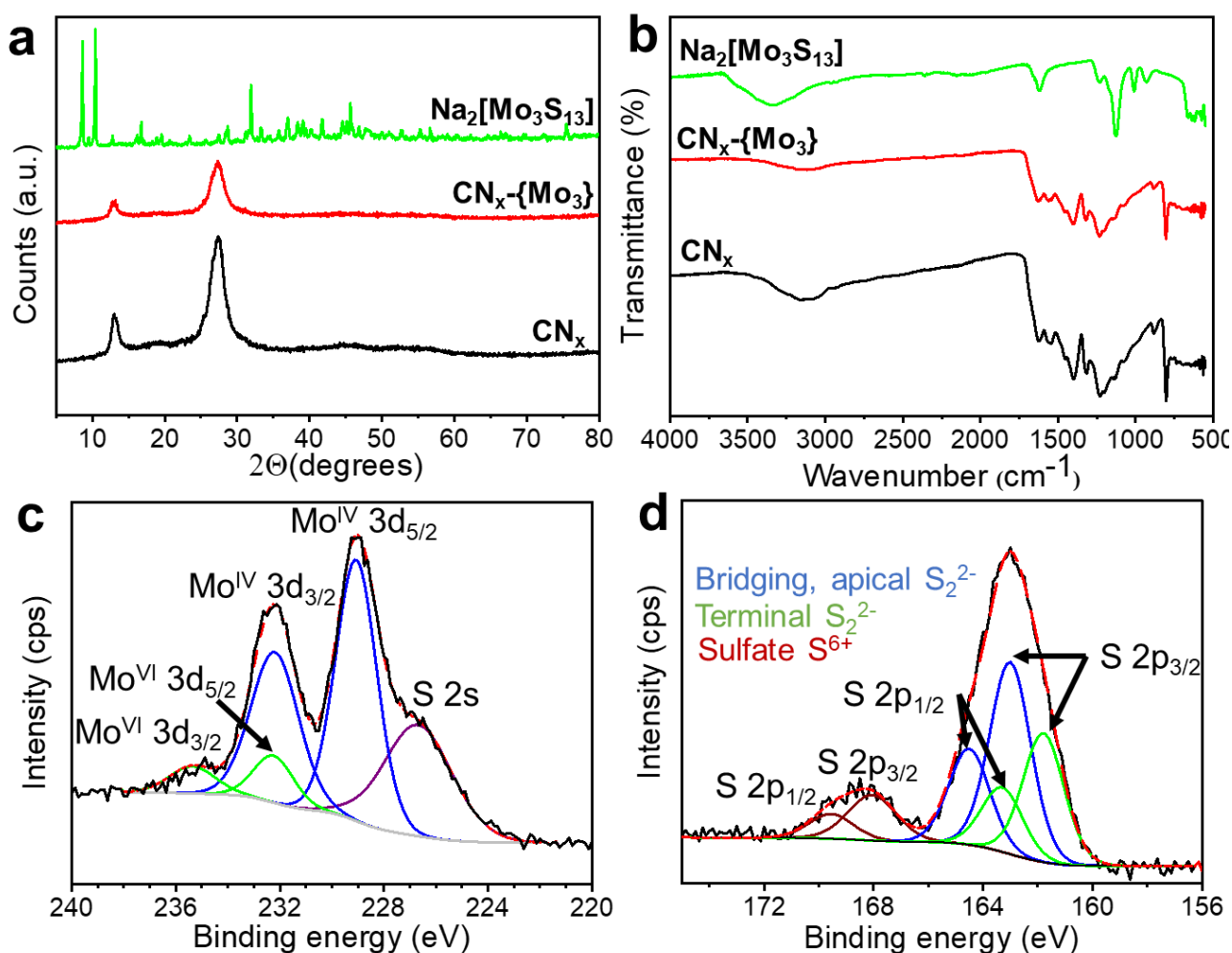
Figure 1. Characterization of materials: (a) XRD patterns; (b) FTIR spectra. Deconvoluted XP spectra in the Mo 3d (c) and S 2p (d) range of CN_x-{Mo_3} (10 wt% loading) photocatalyst.

Figure 2 shows the results of the TEM investigation of CN_x-{Mo_3}. The overview images depict mostly large pieces of amorphous and undefined structure (Fig. 2a), however, crystalline flakes are also detectable in TEM (Fig. 2b). Energy filtered TEM images show a homogeneous distribution of

Mo on the surface of the CN_x material (Fig. 2a). It should be mentioned that the crystalline flakes were amorphized as result of electron irradiation when acquiring elemental maps (Fig. 2c). The diffraction pattern and FFT (fast fourier transform) of the crystalline flakes show first order reflection at 2.2 nm^{-1}, which can be attributed to a polymeric carbon nitride phase (Fig. 2b insets). Elemental mapping performed on the amorphous and crystalline parts of the sample shows uniform distribution of the {Mo$_3$} clusters in CN_x material. We note that {Mo$_3$} deposition leads to a reduction of the specific surface area from 13 down to 5 m^{2}g^{-1}.
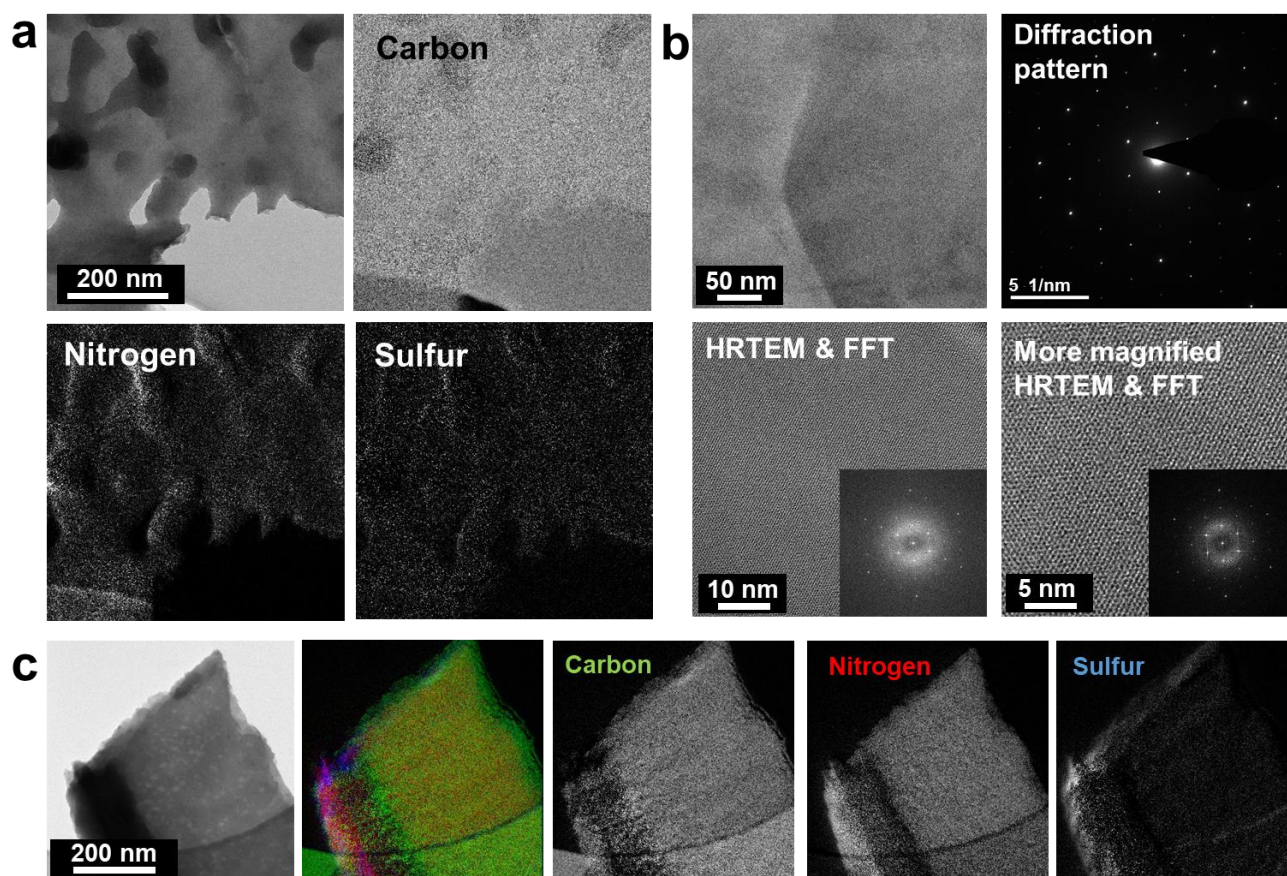
Figure 2. TEM analysis of the amorphous crystalline areas of the CN_x-{Mo$_3$} (10 wt% loading) sample. (a): Bright-field image of the amorphous area and corresponding energy filtered images showing the distribution of carbon, nitrogen and sulfur. (b) Overview image, diffraction pattern and HRTEM images with corresponding local FFT patterns of a crystalline area of the sample. (c) Large overview image and corresponding elemental distributions of a crystalline flake of the sample.

Another indirect indication of the homogeneous distribution of the {Mo$_3$} clusters within CN_x can be obtained from the TG data (Fig. 3a, ESI Fig. S3). The decomposition onset is shifted by ca. 100 °C

towards the low-temperature region for the CN_x-{Mo_3} sample as compared to pristine CN_x (Fig. 3a). This increase of the thermal decomposition rate of the hybrid is due to the solid acid-catalyzed effect of the highly dispersed {Mo_3} clusters or Mo oxides, which might be formed under thermal treatment in air. A similar effect was also reported for other metal oxide-doped polymeric carbon nitride systems.[34]

The optical absorption edge of CN_x remains the same after the incorporation of the {Mo_3} clusters (Fig. 3b); the only additional feature is a broad absorption tail in the visible region that can be attributed to electronic transitions within finely distributed {Mo_3} clusters.
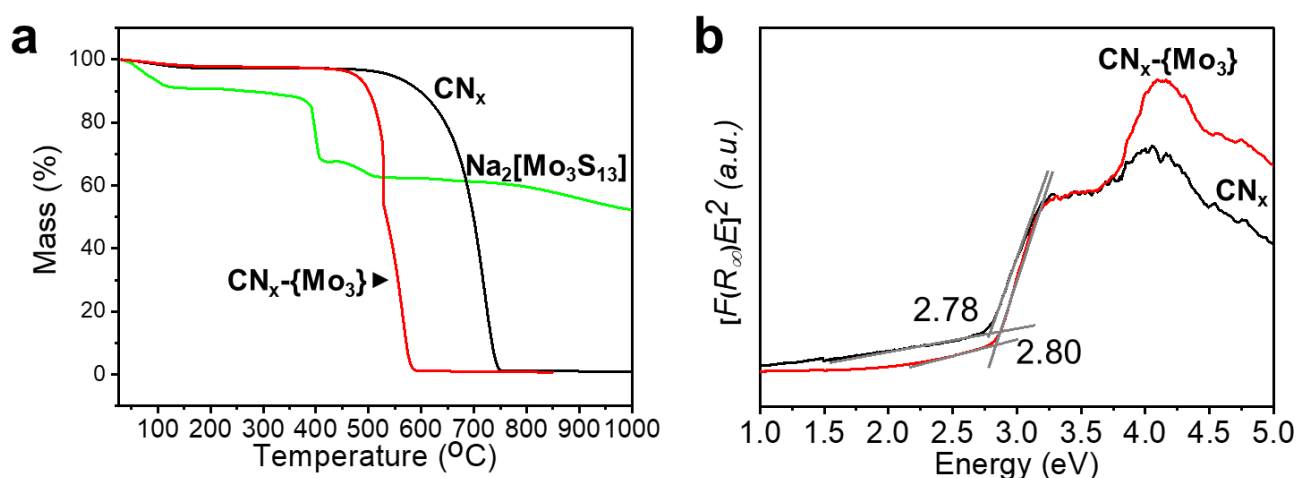
Figure 3. (a) Thermogravimetric analysis of the prepared materials in air and (b) Tauc-plots of the studied CN_x photocatalysts with and without {Mo_3} clusters (10 wt% loading).

Light-driven hydrogen evolution

The importance of ultrasonication during the depostition of co-catalyst is illustrated by the increased activity of the ultrasonicated materials in photocatalytic HER (ESI, Fig. S4). Henceforth, this procedure was applied to all photocatalysts discussed below. Preliminary experiments were performed to establish the optimal conditions for carrying out photocatalytic HER reactions in suspensions of the prepared materials. These initial investigations showed that optimum {Mo_3} cluster loading onto CN_x was 10 wt% (ESI, Fig. S1), and subsequently other conditions were optimized for the CN_x-{Mo_3} sample permitting it to attain its highest activity using 10 mg of the photocatalyst in 10 ml of a H_2O:MeOH (9:1, v:v) solution with near neutral pH. The presence of 10%

MeOH in the reaction medium, apart from playing a role of sacrificial reducing agent, also inhibits ligand-exchange reaction of the {Mo$_3$} cluster, where surface S_2^{2-} might be gradually exchanged with hydroxide or water ligands.[27] The pristine carbon nitride sample (CN$_x$) does not show any significant H$_2$ evolution activity under given conditions (Fig. 4a), while the CN$_x$-{Mo$_3$} is clearly active in this reaction. Few points are noteworthy in this context. Firstly, {Mo$_3$} clusters trigger the photocatalytic H$_2$ evolution even in the presence of methanol, a much weaker reducing agent than lactic acid used by Wang *et al.*[25] Not surprisingly, the activity towards H$_2$ evolution can be enhanced by the application of additional electron donor such as ascorbic acid (ESI, Fig. S5, Fig. 4b). Furthermore, though the activity of CN$_x$-{Mo$_3$} is well below that of the benchmark Pt-CN$_x$ (Fig. 4a), we note that platinum is more expensive than molybdenum by the factor of ~1000, which eventually might become a determinative factor for the development of such systems. Interestingly, addition of an alternative widely used sacrificial reducing agent, triethanolamine (TEOA), lowered the yield of H$_2$ (Fig. 4b), which can be explained by the decomposition of {Mo$_3$} clusters in the highly basic solution of TEOA.
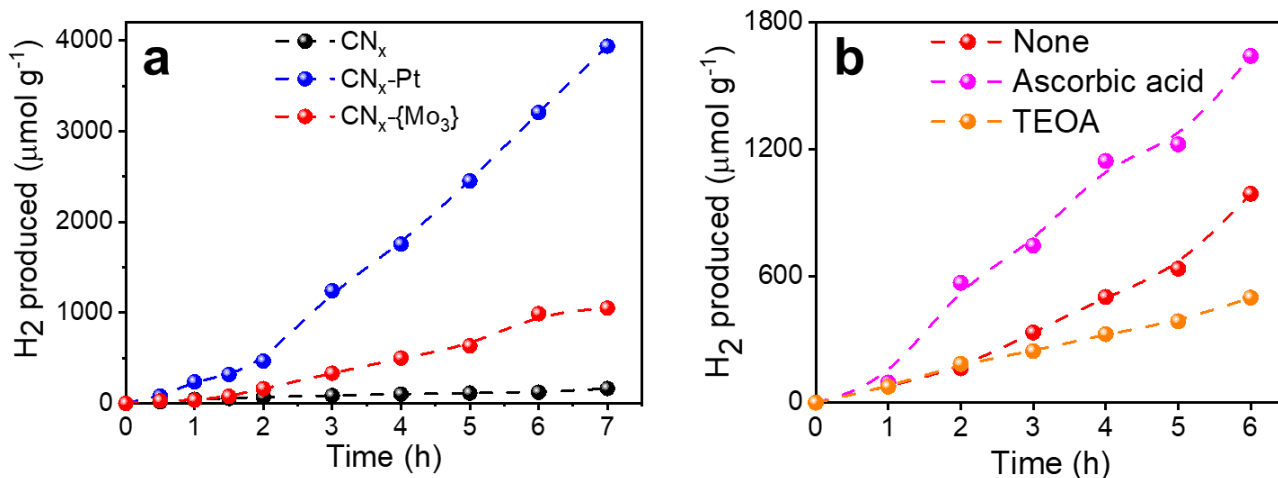

Figure 4: Photocatalytic HER performed using CN$_x$ based materials under 420 nm irradiation. Conditions: [catalyst] : 10mg, Solvent: 10 ml H$_2$O:MeOH (9:1, v:v), (a) in absence and (b) presence of additional electron donors [Triethanolamine] : 10% or [Ascorbic Acid] : 0.1 M.

Optical spectroscopy of CN$_x$-{Mo$_3$}

To investigate the excitonic processes involved in the system, we performed steady-state photoluminescence (PL), time-resolved PL and fs-transient absorption (fs-TA) measurements.

Figures 5a,b depict the photoluminescence properties of pristine CN_x and CN_x-$\{Mo_3\}$ upon 380 nm excitation. All samples show identical photoluminescence spectra peaking at 440 nm corresponding to optical bandgap emission. Compared to pristine CN_x, addition of $\{Mo_3\}$ at the loading of 10 wt% and 20 wt% quenches the emission, which indicates an enhanced separation efficiency of the photoinduced charge carriers at the interface of higher loading samples. However, at a very low loading (2 wt%), we observed an increase of the emission intensity. In order to explain this finding, we propose that the addition of few $\{Mo_3\}$ clusters leads to a situation in which the negatively charged clusters preferentially interact with the amine groups thereby breaking the amine hydrogen bonds with water or/and heptazine nitrogen atoms. The amine groups are apparently associated with shallow trapping states,[35,36] which upon addition of only 2 wt% $\{Mo_3\}$ shift in energy and can thermally repopulate emissive excitonic states. This is in line with the increase of the photoluminescence lifetime from 3.02 (pristine CN_x) to 5.49 ns (upon addition of 2 wt% $\{Mo_3\}$). The dropping photoluminescence intensity in 10 wt% CN_x-$\{Mo_3\}$ correlates with the shortened emission lifetime, which drops back to 3.18 ns. This indicates that, while the radiative rates of 2 wt% and 10 wt% CN_x-$\{Mo_3\}$ remain comparable, the addition of larger number of $\{Mo_3\}$ clusters leads to an increased non-radiative decay of the bandgap emission. Such non-radiative decay channel is likely associated with the dissociation of band-edge or shallow trapped excitons into charge carriers at the CN_x-$\{Mo_3\}$ interfaces. Considering the non-radiative decay in 10 wt% CN_x-$\{Mo_3\}$ to consist of an intrinsic non-radiative decay channel, which is also present in 2 wt% CN_x-$\{Mo_3\}$ and an additional decay channel induced by the increased cluster concentration, one can consider $k_{nr}^{10wt\%} = k_{nr}^{2wt\%} + k_{nr}^{\{Mo_3\}}$. Based on the photoluminescence decay times and under the assumption that the radiative rates remain unchanged one yields $k_{nr}^{\{Mo_3\}} = 13.2 \cdot 10^7 /sec$, which can be considered the rate of cluster induced charge carrier generation from shallow trapped excitons in 10 wt% CN_x-$\{Mo_3\}$.
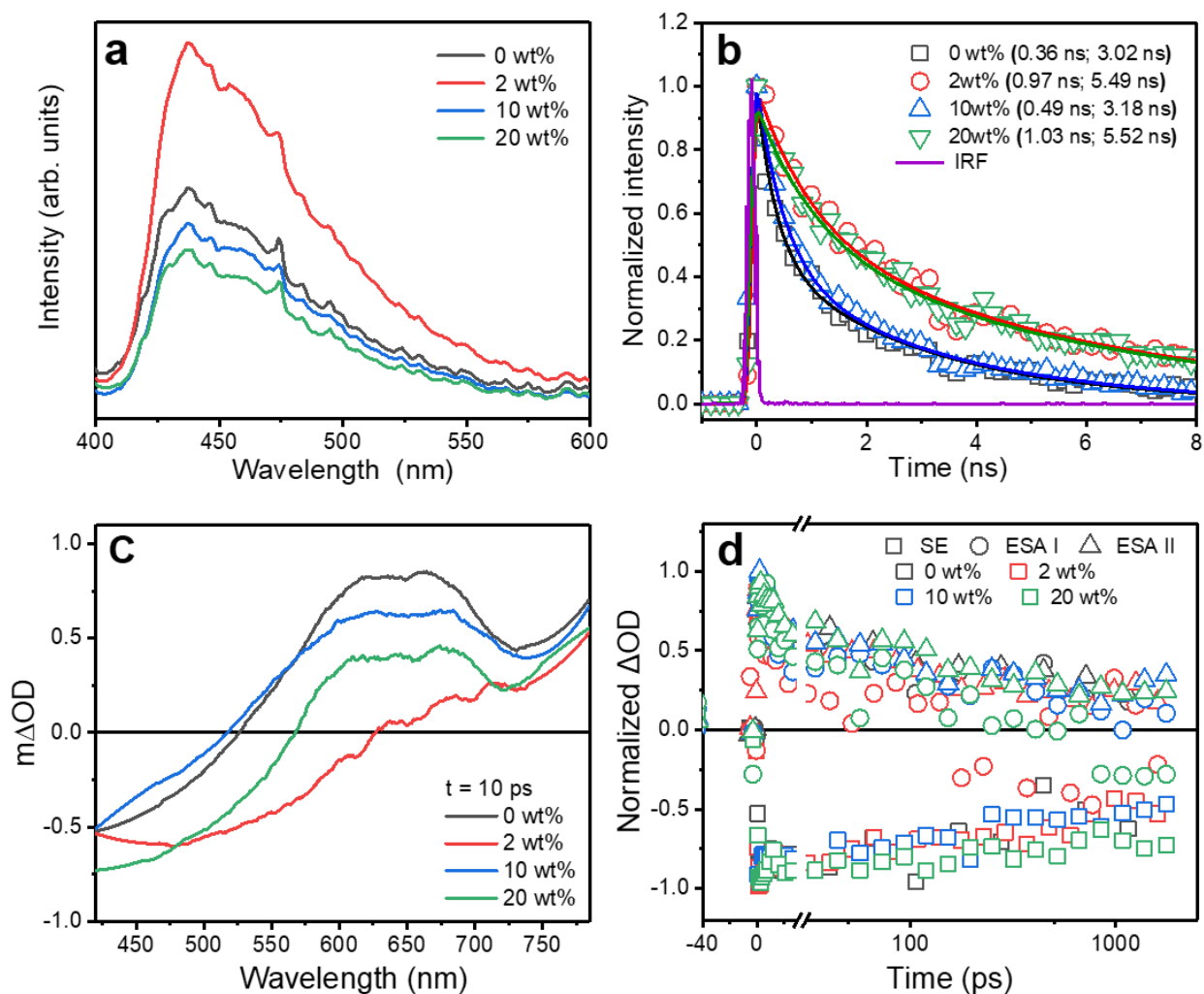
Figure 5: (**a**) Steady-state photoluminescence spectra of CN_x suspensions at different loading ratios of {Mo$_3$}. The spectra were recorded upon excitation at 380 nm. (**b**) Time-resolved photoluminescence decay curves of {Mo$_3$} functionalized CN_x suspensions (2mg mL^{-1}) after 385 nm photoexcitation. The photoluminescence decay curves were generated by spectrally integrating streak camera data between 410 and 550 nm. (**c**) Transient absorption spectra taken upon excitation at 325 nm with a pump-probe delay of 10 ps. The spectra were smoothed by Savitzky-Golay method to reduce high-frequency noise from scattering; the original data are shown in the ESI (Figure S6). (**d**) fs-transient absorption decay kinetics of CN_x materials dispersed in H_2O upon 325 nm excitation. The pump pulses carried an energy of 0.3 µJ per pulse. The transient absorption kinetics depicted were generated by spectrally integrating the transient absorption data in the probe wavelength ranges indicated in panel (**c**). GSB = ground state bleach; SE = stimulated emission; ESA = excited-state absorption.

Upon increasing the loading to 20 wt% {Mo$_3$}, the lifetime of the emission increases again (to 5.52 ns) while the emission yield, as indirectly reflected in the photoluminescence intensity remains constant at best. Assuming that the non-radiative rates associated with charge generation are at least as high as in 10 wt% {Mo$_3$}, we have to conclude that the radiative rate drops upon increasing the cluster loading.

This illustrates that high catalyst loading impacts the electronic structure of the underlying CN_x material causing the radiative rates to drop. It should be pointed out that the discussion laid out before is based on the two long lifetimes obtained from the bi-exponential fit of the photoluminescence decay. Figure S8 in ESI depicts the spectral components associated with the few-ns component and the sub-ns component. Considering the spectral characteristics of the components, we conclude that the blue-shifted short-lived photoluminescence stems from the band-edge emission, while the slower component reflects the decay of weakly trapped excitons.[37] In addition to the discussion above, we observe that the overall weight of the short-lived component to the time-resolved photoluminescence data decreases upon addition of {Mo_3} clusters to the CN_x material. We associate this trend with an increased probability of bandgap exciton quenching by {Mo_3} cluster-induced charge separation.

Next, we will consider fs transient absorption data recorded for the differently loaded CN_x materials upon excitation at 325 nm. Given the specific experimental setup, the data are recorded up to delay times of 1.8 ns. The transient absorption spectra recorded at a pump-probe delay of 10 ps (see Figure 5c) show a region of negative feature, which contains contributions from ground state bleach (GSB) and stimulated emission (SE) and two excited-state absorption (ESA) features, one at roughly 650 nm and one peaking towards the near-IR. The contribution from SE is apparent when comparing the shape of the negative transient absorption feature: for 2 wt% {Mo_3}, the sample with the highest emission intensity, the negative band extends furthest to the red and partially overlaps with the visible ESA band (which we refer to as ESA I).

To compare the photoinduced kinetics for the different materials, the characteristic transient absorption signals, *i.e.* GSB, the ESA in the visible and near-IR regions (Figure 5c), are spectrally integrated in the respective wavelength ranges. The resultant kinetics are normalized and depicted in Figure 5d. It is apparent that the addition of the {Mo_3} catalysts does not impact the ultrafast photoinduced kinetics in the CN_x materials. Similar results are also observed for CN_x samples loaded with Pt-nanoparticles as a catalyst (see Figure S7), where the time resolved PL and transient absorption data do not show any significant changes compared to experiments done with CN_x alone.

The data for the CN$_x$-Pt samples can also be understood in terms of an excited state decay following a power-law dependence and thus implying a trap-assisted recombination process.[38-40] This is reminiscent of the results obtained for polymeric carbon nitride modified with Pt *via* photodeposition.[40]

Photopotential transient measurements

While the fs transient absorption data indicate ultrafast photoinduced kinetics (on ps timescale), which are not notably affected by the molecular {Mo$_3$} catalyst, our photoluminescence quenching experiments revealed that the addition of larger amounts of {Mo$_3$} catalyst is likely associated with the dissociation of the band-edge and/or shallow trapped excitons into charge carriers, *i.e.* to increased charge separation. Furthermore, we observed a significant effect of the catalyst on the photocatalytic turnover (Figure 4). As the catalysis typically occurs on a rather slow time scale, we envisaged that the catalyst effects could be possibly followed by open-circuit photopotential transient measurements.[41-44] Indeed, this is the case as evidenced by the stark difference in photopotential transients recorded for CN$_x$ powders (with and without catalysts) after deposition onto FTO glass (Fig. 6a). In such a system, the sign of the photopotential is determined by the competitive kinetics of electron and hole transfers at the FTO/CN$_x$ and CN$_x$/(catalyst)/solution interfaces. The very small values of the photopotentials, as compared to conventional semiconductors, are related to the strongly insulating character of polymeric CN$_x$,[45] and to the rather low quality of electric contact between CN$_x$ and FTO. Notably, pristine CN$_x$ without any catalyst exhibits small *negative* photopotentials, meaning that the photogenerated electrons do not readily react with the electrolyte, but are instead accumulated in CN$_x$ and in the underlying FTO substrate. In contrast, after introducing the catalysts, either Pt or {Mo$_3$}, the photopotential behaviour is completely reversed and the photopotentials are *positive* now. This shows that, in the presence of the catalyst, the photogenerated electrons are more effectively extracted by the catalyst − as already corroborated by the observed decrease of the photoluminescence intensity and increase of the non-radiative decay into the charge separated state − and channelled to protons in solution, while the oxidizing equivalents (holes) are accumulated in

CN$_x$ and shift the Fermi level of the FTO to more positive potentials (Fig. 6b). This experiment clearly confirms, in analogy to conventional Pt hydrogen evolution catalyst,[46] the strong effect of molecular {Mo$_3$} clusters on exciton dissociation and unidirectional transfer of trapped electrons from CN$_x$ to protons in the solution.
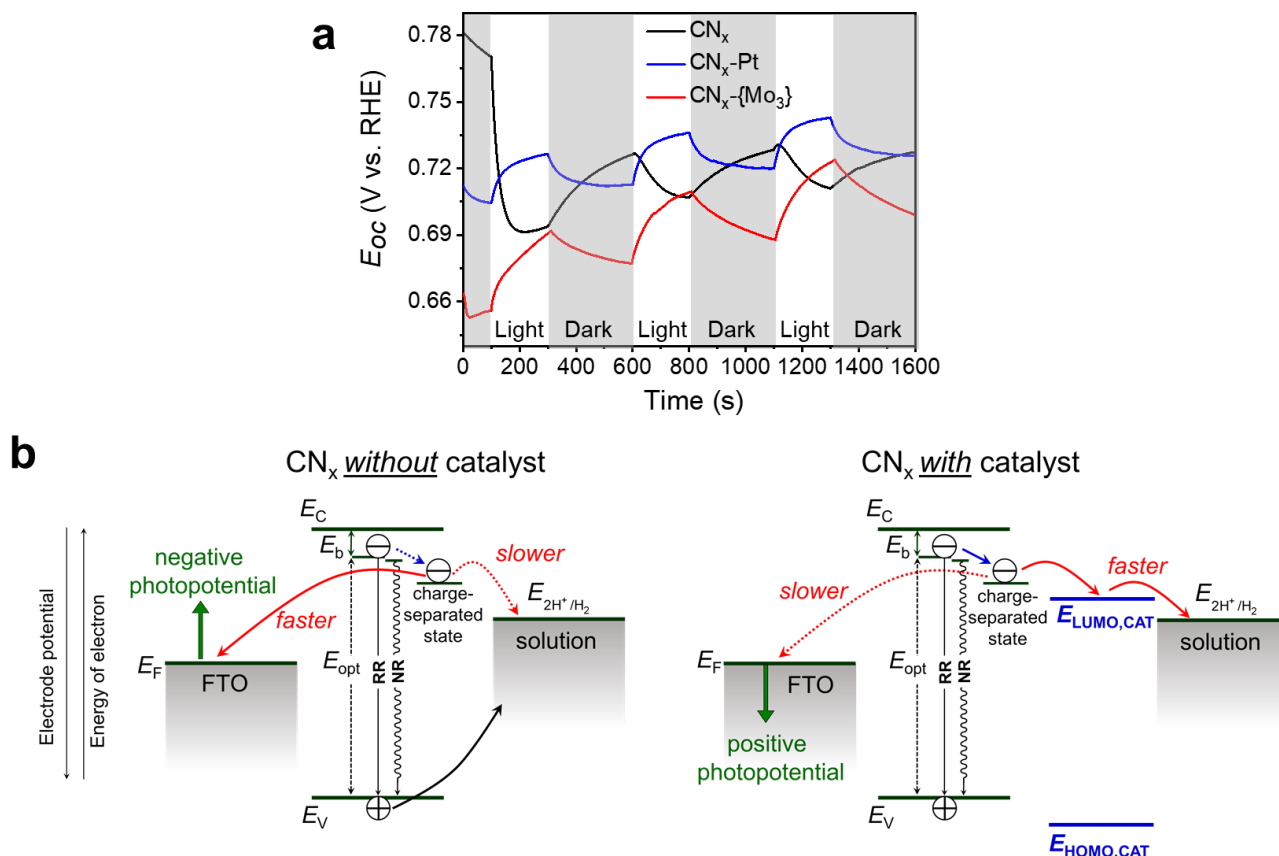

Figure 6. (a) Open-circuit photopotential measurements of the CN$_x$, CN$_x$-Pt and CN$_x$-{Mo$_3$} samples recorded in an aqueous LiClO$_4$ (0.1 M; pH 7) electrolyte (the solution was purged with argon prior to experiments); the materials were deposited on FTO and irradiated from the backside with monochromatic light (λ = 380 nm); **(b)** A simplified scheme showing the generation of photopotential at FTO/CN$_x$ photoelectrodes without and with the {Mo$_3$} catalyst: E_c and E_v stand for the conduction and valence band edge of CN$_x$; **RR** and **NR** stand for radiative and non-radiative recombination from emissive (band-edge) and non-emissive (shallow-trap) excitonic states, respectively; other recombination pathways are omitted for the sake of clarity; E_{opt} designates the optical bandgap of CN$_x$, E_b stands for the exciton binding energy and was estimated as ~0.3 eV according to Ref. [46], the HOMO-LUMO gap of the catalyst has been estimated as 2.5 eV by DFT calculations (see the ESI for details).

Conclusions

The electron accumulation in polymeric carbon nitride photocatalysts is known to be one of the major bottlenecks in light-driven hydrogen evolution,[47,48] and has been typically addressed by deposition of

Pt,[48-50] Ni-based molecular catalysts,[51-53] or enzymes.[11,54] We investigated polymeric carbon nitride coupled with thiomolybdate $\{Mo_3\}$ clusters as an inexpensive alternative to widespread Pt-containing systems. The $\{Mo_3\}$ clusters do promote the hydrogen evolution reaction under visible light irradiation in the presence of methanol or other (stronger) reducing agents, yet the activity of CN_x-$\{Mo_3\}$ composites was found to be significantly lower than that of CN_x-Pt benchmark photocatalysts. While the deposition of the $\{Mo_3\}$ clusters does not induce any significant structural alteration of the polymeric carbon nitride absorber, the loading of the $\{Mo_3\}$ catalyst exerts an influence on exciton and charge transfer dynamics. At sub-optimal (low) $\{Mo_3\}$ cluster loadings the excitons are trapped in shallow states within a few ns. These non-emissive excitonic states (shallow traps) are apparently in a thermal equilibrium with band-edge emissive states leading to enhanced photoluminescence. At higher $\{Mo_3\}$ catalyst loading, the transient PL measurements show that the excitons dissociate more effectively, forming thus more populated charge-separated (deep trap) states. This is followed by more efficient electron transfer to the catalyst and protons in the solution, as indicated by the change of the sign of the open-circuit photopotential to positive (Fig. 6b). Finally, three points are noteworthy. First, the charge transfer to the catalyst, both molecular $\{Mo_3\}$ clusters and Pt nanoparticles, definitely occurs on a relatively longer (ns-s) time scale, as neither $\{Mo_3\}$ nor Pt catalysts had impact on the ultrafast (sub-ns) photoinduced kinetics in the CN_x materials. These results are consistent with recent reports by Durrant et al,[47] suggesting that generation of "long-lived" (> ns time scale) electrons is beneficial for enhancing the photoactivity in hydrogen evolution. Second, while the charge-separated deep trap states play an important role in the CN_x-$\{Mo_3\}$ system by facilitating the exciton dissociation, it cannot be ruled out that they also act as recombination centers, which – in view of further improvements on photocatalytic activity of carbon nitrides – makes an elaborated engineering of their electronic and interfacial properties mandatory. Third, as the emissive decay kinetics shows an obvious deviation from pristine CN_x at non-optimal catalyst loadings (2 and 20 wt%) but not in case of the optimal loading (10 wt%), the design and development

of appropriate synthetic strategies for optimizing the catalyst loading without affecting negatively the electronic structure of the CN_x materials is essential for enhancing the photoconversion efficiencies.

Author contributions

T.J., C.S., B.D., D.M. and R.B. conceived the research and lead the project. A.R., E.A., D.M., C.A. and I.K. performed the synthesis and characterization of materials, interpreted all data, and wrote the manuscript. J.B. and U.K. performed the TEM measurements and analysis. T.D. performed the XPS analysis. C.L. and B.D. performed the spectroscopy studies. J.B. and U.K. performed TEM characterization. C.I. and T.J. performed theoretical calculations. All authors wrote and commented on the manuscript.

Conflict of interests

The authors declare no competing interests.

Acknowledgements

References

1. J. Barber, *Sustainable Energy Fuels.*, 2018, **2**, 927-935.

2. A. Kudo and Y. Miseki, *Chem. Soc. Rev.*, 2009, **38**, 253-278.

3. X. Chen, S. Shen, L. Guo and S. S. Mao, *Chem. Rev.*, 2010, **110**, 6503-6570.

4. G. Zhang, Z.-A. Lan and X. Wang, *Angew. Chem., Int. Ed.*, 2016, **55**, 15712-15727.

5. M. F. Kuehnel and E. Reisner, *Angew. Chem., Int. Ed.*, 2018, **57**, 3290-3296.

6. X. Zou and Y. Zhang, *Chem. Soc. Rev.*, 2015, **44**, 5148-5180.

7. X. Wang, K. Maeda, A. Thomas, K. Takanabe, G. Xin, J. M. Carlsson, K. Domen and M. Antonietti, *Nat. Mater.*, 2009, **8**, 76-80.

8. X. Wang, K. Maeda, X. Chen, K. Takanabe, K. Domen, Y. Hou, X. Fu and M. Antonietti, *J. Am. Chem. Soc.*, 2009, **131**, 1680-1681.

9. N. Wang, J. Wang, J. Hu, X. Lu, J. Sun, F. Shi, Z.-H. Liu, Z. Lei and R. Jiang, *ACS Appl. Energy Mater.*, 2018, **1**, 2866-2873.

10. K. Maeda, X. Wang, Y. Nishihara, D. Lu, M. Antonietti and K. Domen, *J. Phys. Chem. C*, 2009, **113**, 4940-4947.

11. C. A. Caputo, M. A. Gross, V. W. Lau, C. Cavazza, B. V. Lotsch and E. Reisner, *Angew. Chem., Int. Ed.*, 2014, **53**, 11538-11542.

12. J. Wang, J. Chen, P. Wang, J. Hou, C. Wang and Y. Ao, *Appl. Catal. B: Environ.*, 2018, **239**, 578-585.

13. Y. Wu, H. Wang, W. Tu, S. Wu, Y. Liu, Y. Z. Tan, H. Luo, X. Yuan and J. W. Chew, *Appl. Catal. B: Environ.*, 2018, **229**, 181-191.

14. Y. Hou, Y. Zhu, Y. Xu and X. Wang, *Appl. Catal. B: Environ.*, 2014, **156-157**, 122-127.

15. L. Ge, C. Han, X. Xiao and L. Guo, *Int. J. Hydrogen Energy*, 2013, **38**, 6960-6969.

16. J. Kibsgaard, T. F. Jaramillo and F. Besenbacher, *Nat. Chem.*, 2014, **6**, 248-253.

17. H. I. Karunadasa, E. Montalvo, Y. Sun, M. Majda, J. R. Long and C. J. Chang, *Science*, 2012, **335**, 698-702.

18. T. F. Jaramillo, K. P. Jørgensen, J. Bonde, J. H. Nielsen, S. Horch and I. Chorkendorff, *Science*, 2007, **317**, 100-102.

19. K. Du, L. Zheng, T. Wang, J. Zhuo, Z. Zhu, Y. Shao and M. Li, *ACS Appl. Mater. Interfaces*, 2017, **9**, 18675-18681.

20. Y. Shang, X. Xu, B. Gao and Z. Ren, *ACS Sustainable Chem. Eng.*, 2017, **5**, 8908-8917.

21. Y. Shang, X. Xu, Z. Wang, B. Jin, R. Wang, Z. Ren, B. Gao and Q. Yue, *ACS Sustainable Chem. Eng.*, 2018, **6**, 6920-6931.

22. M.-L. Grutza, A. Rajagopal, C. Streb and P. Kurz, *Sustainable Energy Fuels.*, 2018, **2**, 1893-1904.

23. D. Recatalá, R. Llusar, A. L. Gushchin, E. A. Kozlova, Y. A. Laricheva, P. A. Abramov, M. N. Sokolov, R. Gómez and T. Lana-Villarreal, *ChemSusChem*, 2015, **8**, 1299-1299.

24. I. Romanenko, A. Rajagopal, C. Neumann, A. Turchanin, C. Streb and F. H. Schacher, *J. Mater. Chem. A*, 2020, **8**, 6238-6244.

25. F. Guo, Y. Hou, A. M. Asiri and X. Wang, *Chem. Commun.*, 2017, **53**, 13221-13224.

26. A. Rajagopal, F. Venter, T. Jacob, L. Petermann, S. Rau, S. Tschierlei and C. Streb, *Sustainable Energy Fuels.*, 2019, **3**, 92-95.

27. M. Dave, A. Rajagopal, M. Damm-Ruttensperger, B. Schwarz, F. Nägele, L. Daccache, D. Fantauzzi, T. Jacob and C. Streb, *Sustainable Energy Fuels.*, 2018, **2**, 1020-1026.

28. Y. Han, D. Yue, M. Kan, Y. Wu, J. Zeng, Z. Bian, Y. Zhao and X. Qian, *Appl. Catal. B: Environ.*, 2019, **245**, 190-196.

29. A. Müller, V. Wittneben, E. Krickemeyer, H. Bögge and M. Lemke, *Z. Anorg. Allg. Chem.*, 1991, **605**, 175-188.

30. R. Siebert, D. Akimov, M. Schmitt, A. Winter, U. S. Schubert, B. Dietzek and J. Popp, *ChemPhysChem*, 2009, **10**, 910-919.

31. M. Ilkaeva, I. Krivtsov, E. Bartashevich, S. Khainakov, J. Garcia, E. Diaz and S. Ordonez, *Green Chem.*, 2017, **19**, 4299-4304.

32. I. Krivtsov, D. Mitoraj, C. Adler, M. Ilkaeva, M. Sardo, L. Mafra, C. Neumann, A. Turchanin, C. Li, B. Dietzek, R. Leiter, J. Biskupek, U. Kaiser, C. Im, B. Kirchhoff, T. Jacob and R. Beranek, *Angew. Chem., Int. Ed.*, 2020, **59**, 487-495.

33. C.-H. Lee, S. Lee, Y.-K. Lee, Y. C. Jung, Y.-I. Ko, D. C. Lee and H.-I. Joh, *ACS Catal.*, 2018, **8**, 5221-5227.

34. Y. He, J. Cai, T. Li, Y. Wu, Y. Yi, M. Luo and L. Zhao, *Ind. Eng. Chem. Res.*, 2012, **51**, 14729-14737.

35. Y. Kang, Y. Yang, L.-C. Yin, X. Kang, L. Wang, G. Liu and H.-M. Cheng, *Adv. Mater.*, 2016, **28**, 6471-6477.

36. X. Li, I. V. Sergeyev, F. Aussenac, A. F. Masters, T. Maschmeyer and J. M. Hook, *Angew. Chem., Int. Ed.*, 2018, **57**, 6848-6852.

37. C. Merschjann, S. Tschierlei, T. Tyborski, K. Kailasam, S. Orthmann, D. Hollmann, T. Schedel-Niedrig, A. Thomas and S. Lochbrunner, *Adv. Mater.*, 2015, **27**, 7993-7999.

38. J. Nelson, *Phys. Rev. B: Condens. Matter Mater. Phys.*, 1999, **59**, 15374-15380.

39. J. J. Walsh, C. Jiang, J. Tang and A. J. Cowan, *Phys. Chem. Chem. Phys.*, 2016, **18**, 24825-24829.

40. R. Godin, Y. Wang, M. A. Zwijnenburg, J. Tang and J. R. Durrant, *J. Am. Chem. Soc.*, 2017, **139**, 5216-5224.

41. D. Monllor-Satoca and R. Gomez, *J. Phys. Chem. C*, 2008, **112**, 139-147.

42. S. Neubert, D. Mitoraj, S. A. Shevlin, P. Pulisova, M. Heimann, Y. Du, G. K. L. Goh, M. Pacia, K. Kruczala, S. Turner, W. Macyk, Z. X. Guo, R. K. Hocking and R. Beranek, *J. Mater. Chem. A*, 2016, **4**, 3127-3138.

43. S. Neubert, P. Pulisova, C. Wiktor, P. Weide, B. Mei, D. A. Guschin, R. A. Fischer, M. Muhler and R. Beranek, *Catal. Today*, 2014, **230**, 97-103.

44. C. Adler, D. Mitoraj, I. Krivtsov and R. Beranek, *J. Chem. Phys.*, 2020, **152**, 244702.

45. M. Bledowski, L. Wang, A. Ramakrishnan, O. V. Khavryuchenko, V. D. Khavryuchenko, P. C. Ricci, J. Strunk, T. Cremer, C. Kolbeck and R. Beranek, *Phys. Chem. Chem. Phys.*, 2011, **13**, 21511-21519.

46. S. Melissen, T. Le Bahers, S. N. Steinmann and P. Sautet, *J. Phys. Chem. C*, 2015, **119**, 25188-25196.

47. W. Yang, R. Godin, H. Kasap, B. Moss, Y. Dong, S. A. J. Hillman, L. Steier, E. Reisner and J. R. Durrant, *J. Am. Chem. Soc.*, 2019, **141**, 11219-11229.

48. V. W.-h. Lau, D. Klose, H. Kasap, F. Podjaski, M.-C. Pignié, E. Reisner, G. Jeschke and B. V. Lotsch, *Angew. Chem., Int. Ed.*, 2017, **56**, 510-514.

49. D. J. Martin, K. Qiu, S. A. Shevlin, A. D. Handoko, X. Chen, Z. Guo and J. Tang, *Angew. Chem., Int. Ed.*, 2014, **53**, 9240-9245.

50. D. J. Martin, P. J. T. Reardon, S. J. A. Moniz and J. Tang, *J. Am. Chem. Soc.*, 2014, **136**, 12568-12571.

51. T. Uekert, H. Kasap and E. Reisner, *J. Am. Chem. Soc.*, 2019, **141**, 15201-15210.

52. H. Kasap, R. Godin, C. Jeay-Bizot, D. S. Achilleos, X. Fang, J. R. Durrant and E. Reisner, *ACS Catal.*, 2018, **8**, 6914-6926.

53. H. Kasap, C. A. Caputo, B. C. M. Martindale, R. Godin, V. W.-h. Lau, B. V. Lotsch, J. R. Durrant and E. Reisner, *J. Am. Chem. Soc.*, 2016, **138**, 9183-9192.

54. C. A. Caputo, L. Wang, R. Beranek and E. Reisner, *Chem. Sci.*, 2015, **6**, 5690-5694.

TOC graphic
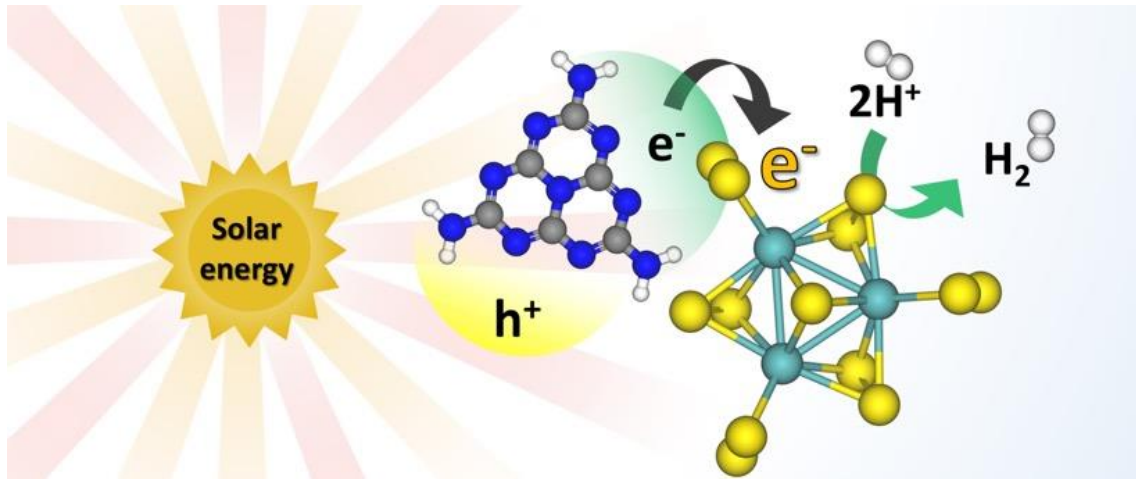
SUPPLEMENTARY INFORMATION

Polymeric carbon nitride coupled with a molecular thiomolybdate catalyst: exciton and charge dynamics in light-driven hydrogen evolution

Ashwene Rajagopal,[a] Elham Akbarzadeh,[a] Chunyu Li,[b,c] Dariusz Mitoraj,[d] Igor Krivtsov,[d,*]

Christiane Adler,[d] Thomas Diemant,[e] Johannes Biskupek,[f] Ute Kaiser,[f] Changbin Im,[d] Magdalena

Heiland,[a] Timo Jacob,[d,g,h] Carsten Streb,[a,g,h]* Benjamin Dietzek,[b,c,i] * Radim Beranek[d,*]

[a]   Institute of Inorganic Chemistry I, Ulm University, Albert-Einstein-Allee 11, 89081 Ulm, Germany

[b]   Institute of Physical Chemistry and Abbe Center of Photonics, Friedrich Schiller University Jena, Lessingstr. 10,
        07743 Jena, Germany

[c]   Department Functional Interfaces, Leibniz Institute of Photonic Technology (IPHT), Albert-Einstein-Str. 9, 07745
        Jena, Germany

[d]   Institute of Electrochemistry, Ulm University, Albert-Einstein-Allee 47, 89081 Ulm, Germany

[e]   Institute of Surface Chemistry and Catalysis, Ulm University, Albert-Einstein-Allee 47, 89081 Ulm, Germany

[f]   Electron Microscopy of Materials Science, Central Facility for Electron Microscopy, Ulm University, Albert-
        Einstein-Allee 11, 89081, Ulm, Germany

[g]   Helmholtz-Institute-Ulm (HIU), Helmholtzstr. 11, 89081, Ulm, Germany

[h]   Karlsruhe Institute of Technology (KIT), P.O. Box 3640, 76021, Karlsruhe, German

[i]   Center for Energy and Environmental Chemistry Jena (CEEC Jena), Philosophenweg 7a, 07743 Jena, Germany

*Corresponding authors: igor.krivtsov@uni-ulm.de, carsten.streb@uni-ulm.de,
    benjamin.dietzek@uni-jena.de, radim.beranek@uni-ulm.de

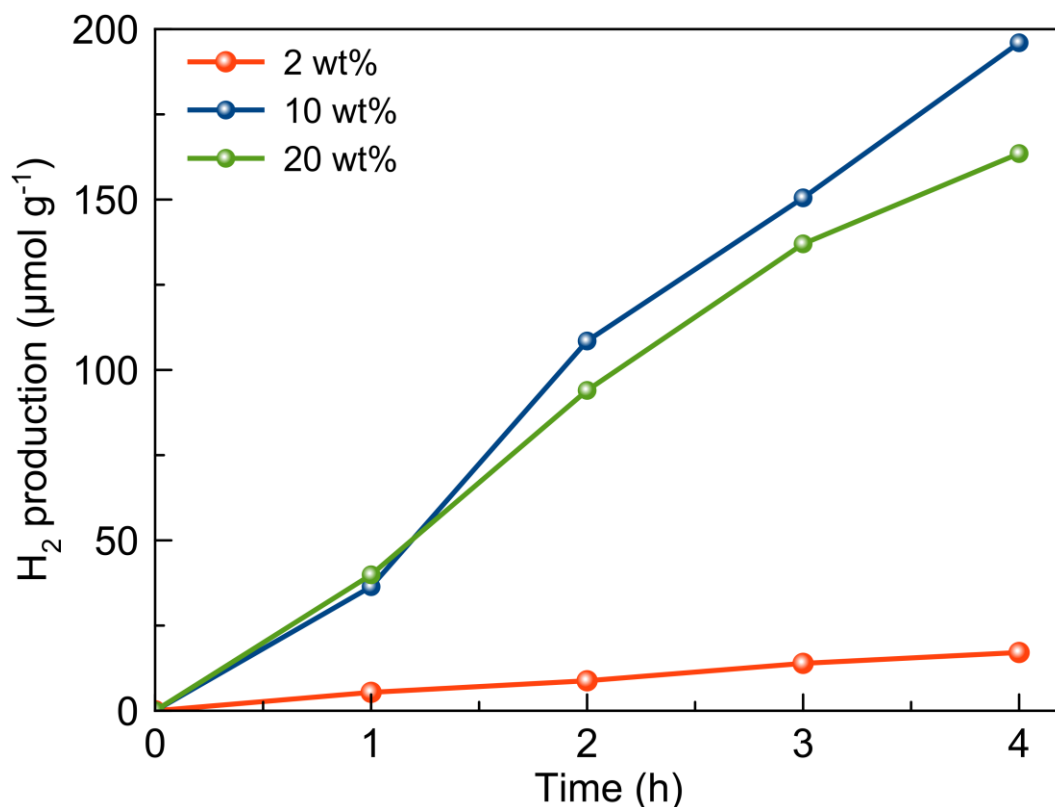## Preliminary photocatalytic study:

Figure S1. Photocatalytic HER performed using CN_x based materials with varied loading of $\{Mo_3\}$ clusters under 420 nm irradiation. Conditions: [catalyst]: 10 mg, Solvent: 10 ml H_2O:MeOH (9:1, v:v). Note that the hydrogen production rates in these preliminary measurements were lower than in the rest of the study due to a difference in geometry of the reaction cell which resulted in different absorbed photon flux.

FTIR analysis:

FT-IR spectra of CN_x, $Na_2[Mo_3S_{13}]$ and $\{Mo_3\}@CN_x$ nanocomposite are displayed in Figure 1b. In the FT-IR spectrum of CN_x and $\{Mo_3\}@CN_x$ hybrid the peaks at around 1639 cm^{1-} can be ascribed to C−N stretching vibration modes and the peaks at 1245, 1329 and 1416 cm^{1-} are attributed to the aromatic C−N stretching. The sharp peak at 806 cm^{1-} is related to the out-of-plane bending vibration of heterocyclic C−N. The broad peak at around 2900−3400 cm^{1-} can be related to the stretching modes of the N−H bond and the hydroxyl group of the adsorbed water. For the pure $Na_2[Mo_3S_{13}]$, the spectrum displays a sharp peak at 1138 cm^{1-} which can be assigned to the SO_4^{2-} group in the compound which probably is produced during the cation exchange process. However, no distinct sign of $[Mo_3S_{13}]^{2-}$ cluster is obvious in the FT-IR spectrum of $\{Mo_3\}@CN_x$ composite, which can be because of the little amount of $\{Mo_3\}$ in the hybrid and also existence of CN_x.
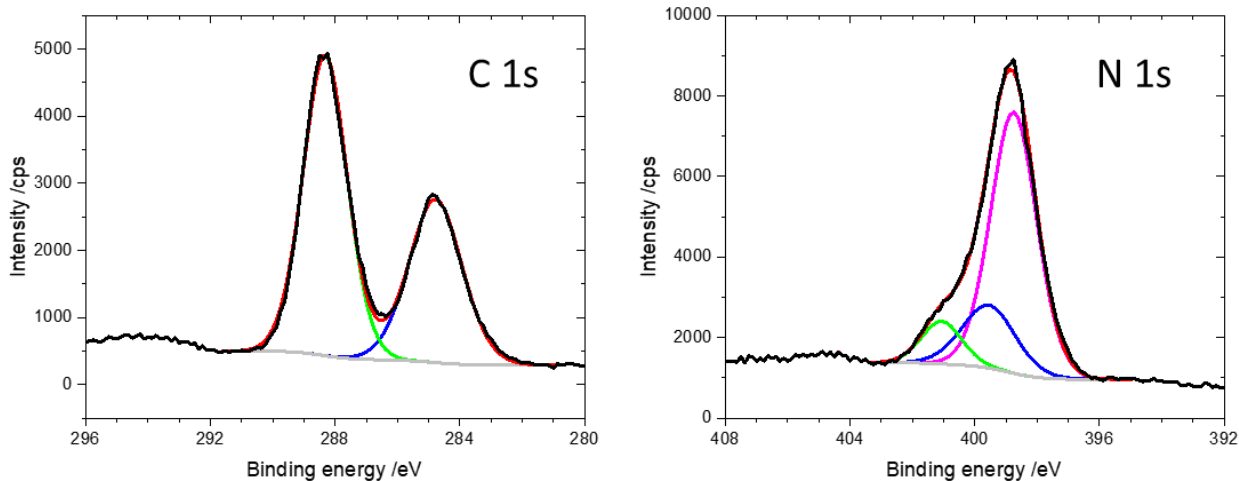
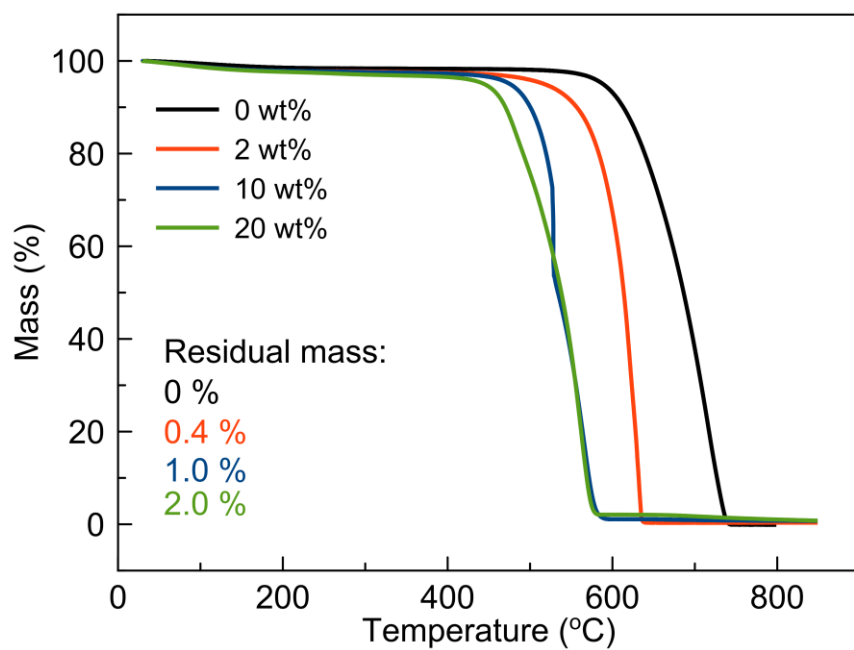**Figure S2**. XPS C 1s and N 1s spectra of CN_x-{Mo_3}

Figure S3. Thermogravimetric analysis of the CN_x materials with different {Mo_3} cluster loadings in air.
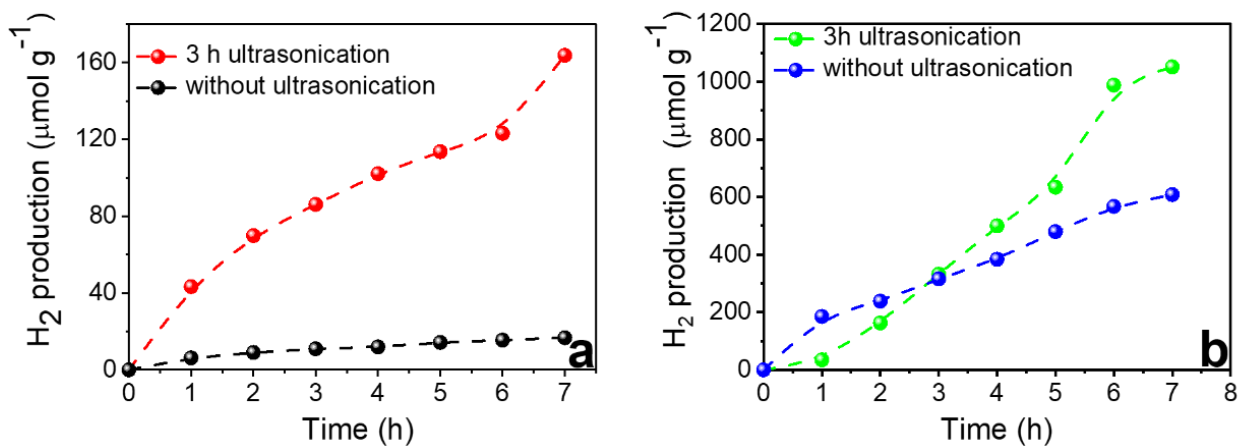
Figure S4. Effect of sonication on photocatalytic HER for (**a**) CN_x and (**b**) CN_x-{Mo_3} under 420 nm irradiation. Conditions: [catalyst] : 10 mg, Solvent: 10 ml H_2O:MeOH (9:1, v:v), in absence of any additional electron donors.
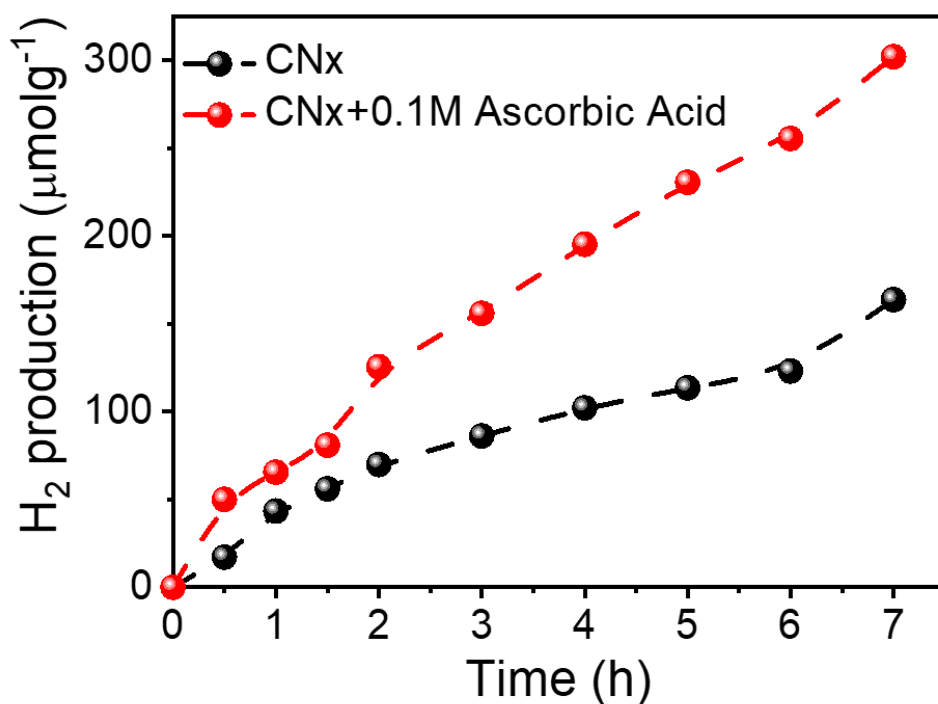

Figure S5. Effect of electron donor addition (0.1M ascorbic acid) on photocatalytic HER in presence of CN_x under 420 nm irradiation. Conditions: [catalyst] : 10 mg, Solvent: 10 ml H_2O:MeOH (9:1, v:v).
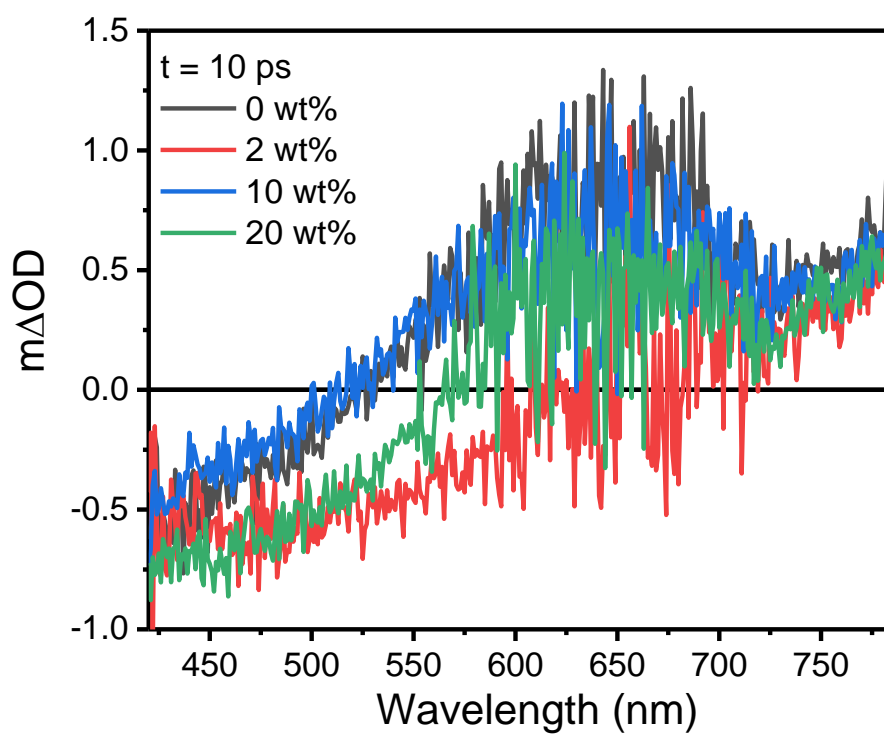
Figure S6. fs-TAS spectra of CN_x-$\{Mo_3\}$ dispersions in H_2O upon excitation at 325 nm at 10 ps delay times. The figure displays the raw data.
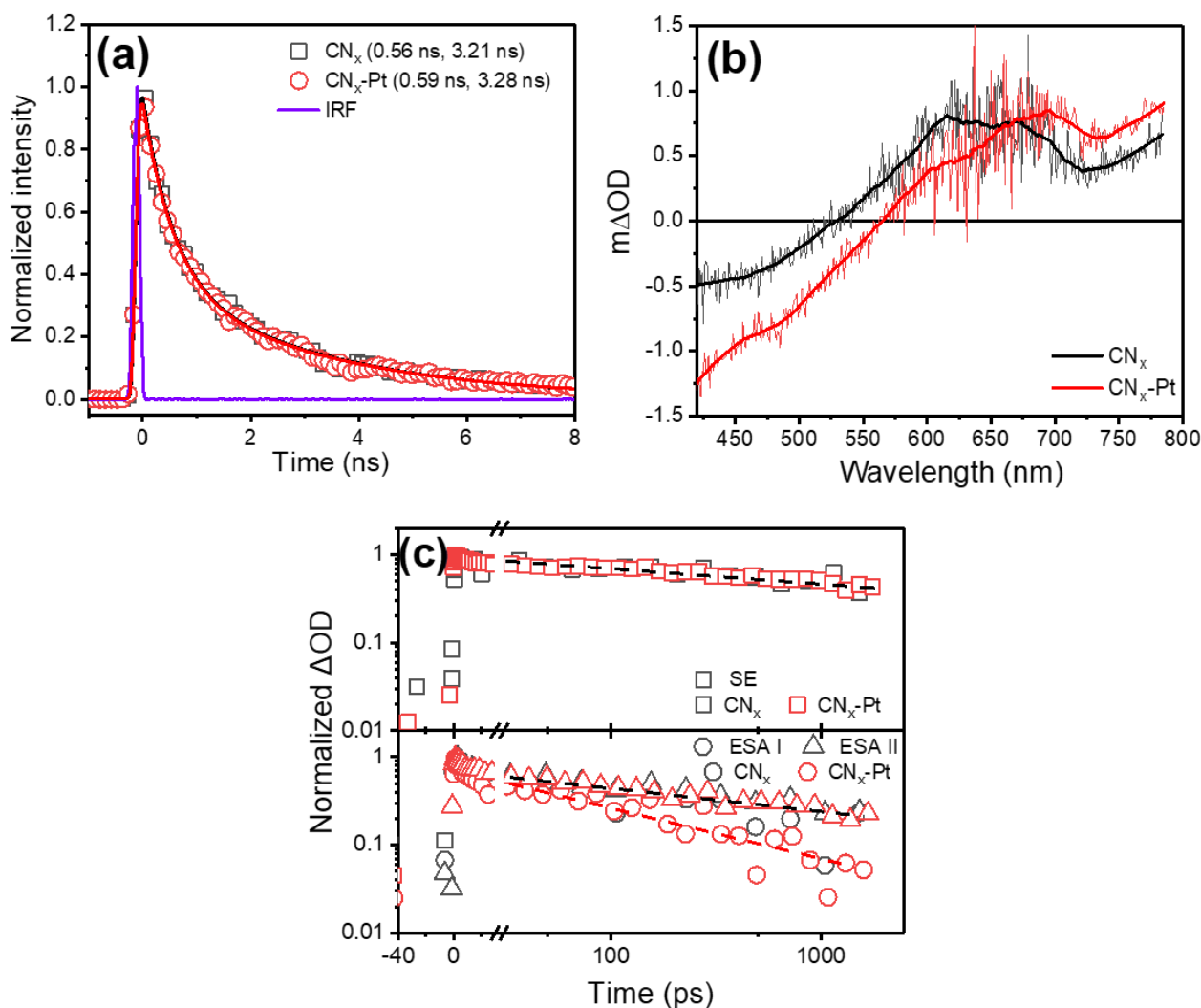
Figure S7. (a) Time-resolved photoluminescence decay curves of Pt functionalized CN_x samples after 385 nm photoexcitation. The samples were prepared by drop casting. (b) fs-TAS spectra at 10 ps delay of CN_x-Pt dispersions in H_2O upon excitation at 325 nm and corresponding (c) fs-TAS decay kinetics obtained by spectrally integrating the transient absorption data in different probe wavelength ranges. A quantitative analysis of the transient absorption data indicates, that the kinetics can be described by a power law model. The exponent of the power law is smaller than unity (~0.43), suggesting that trapping/detrapping plays a significant role in excited state dynamics of the CN_x-Pt samples. This is consistent with the comparably slow time scale for the recombination process.
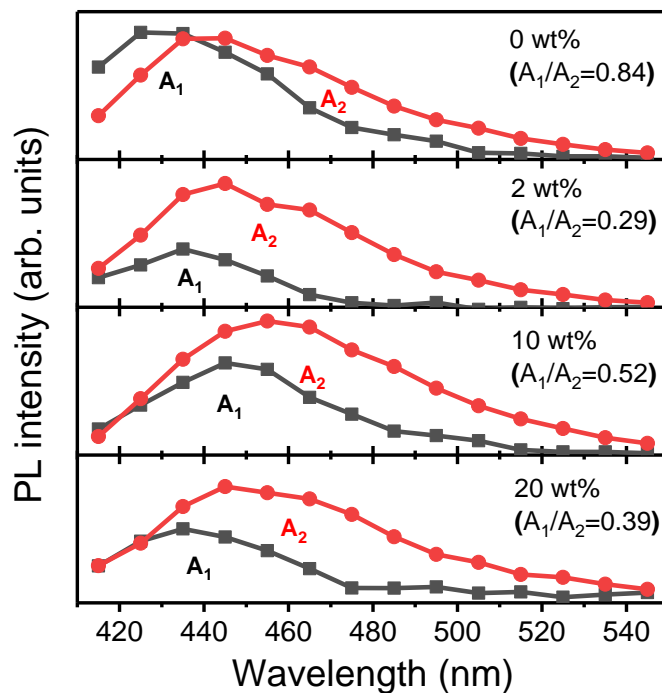
Figure S8. Species-associated emission spectra of CN_x-{Mo_3} with respective lifetimes (black lines present emission from the short-lived photoluminescence ($\tau < 1ns$), while the red spectra reflect the spectra distribution of the long-lived emission with lifetimes ranging from 3.0 to 5.5 ns). The lifetimes are obtained by a global fit of the two-dimensional streak camera data with a biexponential model. The experimental response function of the streak camera measurements is 0.06 ns wide.
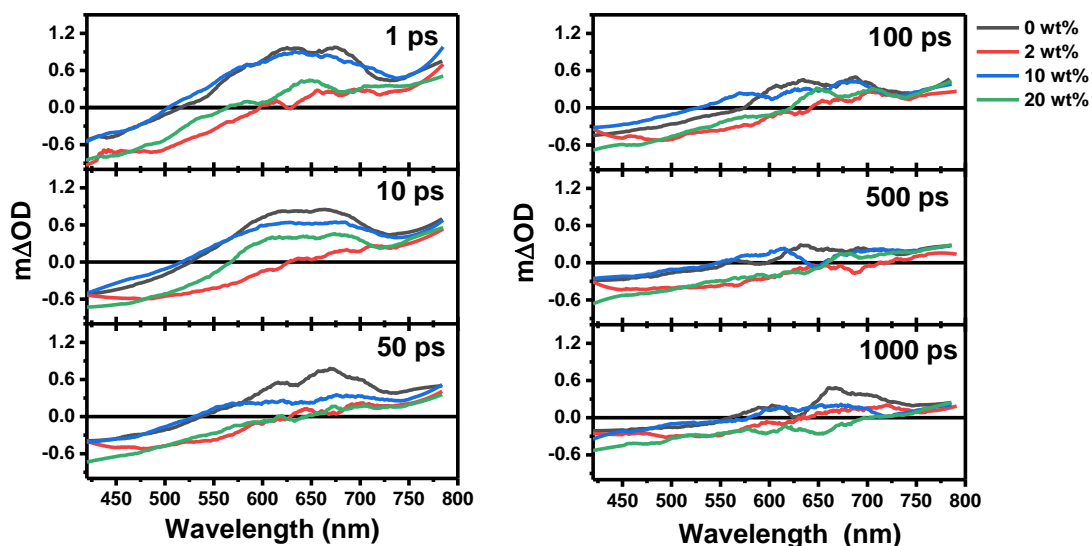

Figure S9. fs-TAS smoothed spectra of CN_x-{Mo_3} dispersions in H_2O. The spectra were recorded upon 325 nm excitation at different delay times.
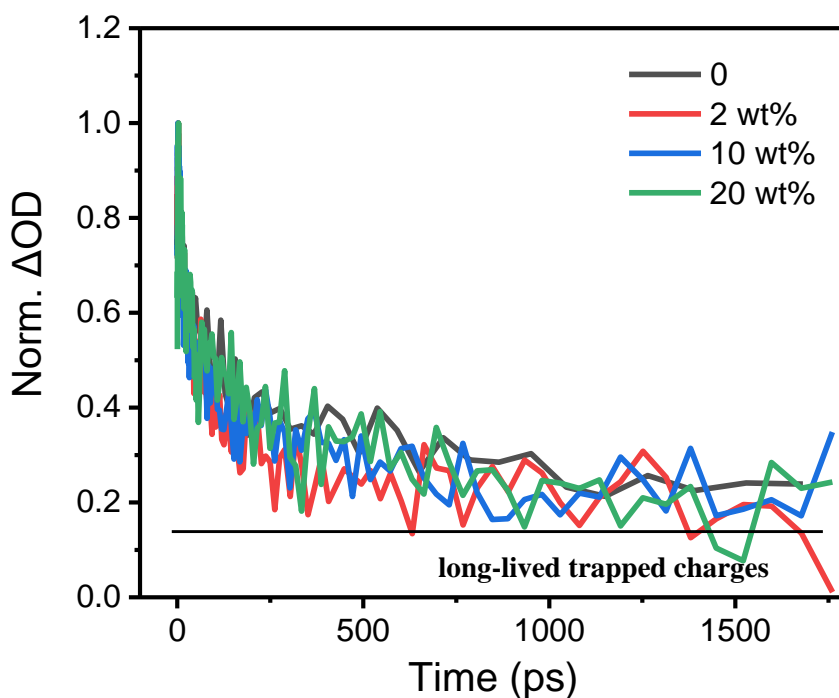
Figure S10. fs-TAS decay of CN_x-$\{Mo_3\}$ dispersions in H_2O integrated within NIR regions upon 325 nm excitation.

Theoretical calculations:

Density Functional Theory (DFT) calculations were performed using the Vienna Ab initio Simulation Package (VASP) version 5.4.4 using the projector-augmented wave (PAW) method to represent the basis set.[1–5] For accuracy of the electronic properties, the Heyd-Scuseria-Ernzerhof (HSE06) hybrid functional was employed.[6, 7] The screening parameter m in HSE was set at 0.2 Å^{-1} and the exchange parameter a was 0.25. Grimme's D3 dispersion correction was used to describe long range dispersive interactions.[8, 9] The wavefunction was optimized to an accuracy of 10^{-6} eV while geometries were relaxed until the forces reached below $5 \cdot 10^{-2}$ eV Å^{-1}. Gaussian finite-temperature smearing was employed with a smearing width of 0.01 eV. A plane wave energy cut-off of 400 eV for both $\{Mo_3\}$ and CN_x. To offset the spurious interactions between the periodic images, vacuum was introduced along the z-direction (~20 Å) for CN_x and $\{Mo_3\}$ was placed to the center of cubic vacuum box (40 Å) with dipole corrections. Integration in the reciprocal space was performed on a 5 x 5 x 1 Monkhorst–Pack *k*-grid mesh. For implicit solvation effects in water, the GLSSA13 solvent model implemented in the VASPsol extension was invoked,[10-12] using a dielectric constant of bulk water at room temperature of 78.4.
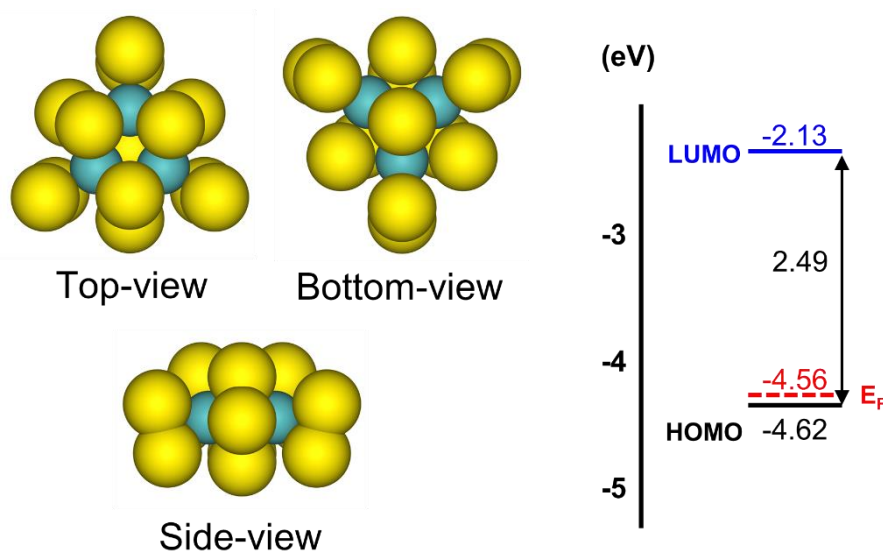
Figure S11. Scheme of the structure {Mo$_3$} employed in DFT calculation and HOMO-LUMO energy.

References

1. G. Kresse, J. Hafner, Phys. Rev. B 1993, 47, 558–561.

2. G. Kresse, J. Hafner, Phys. Rev. B 1994, 49, 14251–14269.

3. G. Kresse, J Furthmüller, Comput. Mater. Sci. 1996, 6, 15–50.

4. G. Kresse, J. Furthmüller, Phys. Rev. B 1996, 54, 11169–11186.

5. G. Kresse, D. Joubert, Phys. Rev. B 1999, 59, 1758–1775.

6. Heyd, J.; Scuseria, G. E.; Ernzerhof, M. J. Chem. Phys. 2003, 118, 8207−8215.

7. Heyd, J.; Scuseria, G. E.; Ernzerhof, M. Erratum: Hybrid Functionals Based on a Screened Coulomb Potential [J. Chem. Phys. 118, 8207 (2003)]. J. Chem. Phys. 2006, 124, 219906.

8. S. Grimme, J. Antony, S. Ehrlich, and S. Krieg, J. Chem. Phys. 2010, 132, 154104.

9. Grimme, S. Ehrlich, and L. Goerigk, J. Comp. Chem. 2011, 32, 1456.

10. D. Gunceler, K. Letchworth-Weaver, R. Sundararaman, K. A. Schwarz, T. A. Arias, Model. Simul. Mater. Sci. Eng. 2013, 21, 074005.

11. K. Mathew, R. G. Hennig, ArXiv160103346 Cond-Mat 2016.

12. K. Mathew, R. Sundararaman, K. Letchworth-Weaver, T. A. Arias, R. G. Hennig, J. Chem. Phys. 2014, 140, 084106.